

# Enhancing $\text{Li}_4\text{Ti}_5\text{O}_{12}$ Anodes for High-Performance Batteries: $\text{Ti}^{3+}$ Induction via Plasma-Enhanced Chemical Vapor Deposition and Dual Carbon/LLZO Coatings

Mohamed M. Abdelaal<sup>[a]</sup> and Mohammad Alkhedher<sup>\*[a]</sup>

Lithium titanium oxide (LTO) is a promising anode material due to its ability to store lithium through intercalation reactions. However, its electrochemical performance is limited by poor electron conductivity and side reactions with the electrolyte. In this study, plasma-enhanced chemical vapor deposition (PECVD) is employed to introduce oxygen vacancies and self-doped  $\text{Ti}^{3+}$  into LTO to improve the internal conductivity. Subsequent carbon coating and aluminum-doped lithium lanthanum zirconate garnet (LLZO) layers resulted in a multi-layered composite denoted as LTO–L-x. Morphological analyses using SEM and TEM demonstrated the successful growth of Al-doped LLZO on carbon-coated LTO. Aluminum ions in LLZO

cubic structure are crucial for stabilizing the high ionic conductive phase during cooling, as confirmed by X-ray diffraction. The dual coating layers have a significant impact on the rate capability, reducing polarization gaps and enabling higher capacities at various current rates. Long-term cycling tests reveal the robustness of the composite, with LTO–L-1.0 retaining 90.8% capacity after 4000 cycles at  $1.0 \text{ A g}^{-1}$ . This underscores the sustained high electronic and ionic conductivity facilitated by the dual coating layers. The study contributes to the design of advanced anode materials for lithium-ion batteries, emphasizing the importance of tailored coating strategies to address conductivity and stability challenges.

## 1. Introduction

Lithium-ion intercalation reactions contribute significantly to the prolonged cycling performance of batteries by preserving the structure of active materials.<sup>[1,2]</sup> Anodes with layered structures, such as graphite, and olivine structures like  $\text{Li}_4\text{Ti}_5\text{O}_{12}$  (LTO), undergo intercalation reactions, making them subjects of extensive literature study.<sup>[2,3]</sup> However, the potential of lithium insertion in graphite is nearly zero, leading to lithium plating, especially at high rates and in cold weather.<sup>[2]</sup> In contrast, LTO, with a potential of around 1.55 V (vs. Li/Li<sup>+</sup>), exhibits minimal volume expansion, providing enhanced safety compared to graphite.<sup>[3,4]</sup> Moreover, LTO can serve as a reference electrode, mitigating issues related to lithium dendrite formation and short-circuits.<sup>[5]</sup>

However, LTO faces challenges such as poor electronic conductivity ( $\sim 10^{-13} \text{ S cm}^{-1}$ ) due to its nature as a metal oxide material.<sup>[6]</sup> This limitation hampers the delivered capacity, particularly at high rates.<sup>[1]</sup> Despite being considered a zero-strain material, LTO experiences lattice structure cracks and continuous degradation during fast charging, affecting cycling stability.<sup>[1,7]</sup> Furthermore, the solid electrolyte interface (SEI) becomes more prone to detachment at high rates, leading to gas evolution at the LTO-electrolyte interface.<sup>[1,8]</sup> Consequently, the degradation of active materials and the ongoing decom-

position of electrolyte components compromise the capacity and cycling stability of LTO.<sup>[7,8]</sup>

To address these challenges, extensive research has been conducted, exploring strategies such as the formation of conductive composites with LTO to enhance electrical conductivity.<sup>[9]</sup> Carbon-coated LTO, for example, increases the electronic conductivity, confines the particles, and creates oxygen vacancies in the active material, resulting in a high capacity retention of 95.0% after 2000 cycles at  $0.5 \text{ A g}^{-1}$ .<sup>[10]</sup> Doping the spinel structure of LTO with different ions has also been explored to enhance ionic conductivity by expanding the lattice parameter.<sup>[11]</sup> Therefore, the corresponding cell volume increases, and lithium-ion movement becomes faster.<sup>[11]</sup> Wu doped larger  $\text{Fe}^{2+}$  ion in the position of  $\text{Ti}^{4+}$  in carbon coated LTO, leading to expanding the cell volume of LTO from 583.141–583.238 Å<sup>3</sup> LTO.<sup>[1]</sup> As a result, the capacity dramatically increased from 60–154 mAh g<sup>-1</sup> for the dual modified Fe-doped and carbon-coated LTO.<sup>[1]</sup> Co-doping  $\text{Mg}^{2+}$  and  $\text{La}^{3+}$  were also used to improve the electron density in LTO lattice and decrease the migration barriers for lithium.<sup>[12]</sup>

Rapid conductive polymers are considered as promising candidates for coating since they allow lithium-ion to move freely at room temperature.<sup>[9]</sup> Wang et.al. coated the ionic conductors  $\text{Li}_{1+x}\text{Al}_x\text{Ti}_{2-x}(\text{PO}_4)_3$  ( $0 < x < 0.5$ ) on LTO to improve the cycling stability and reduce the side reaction with electrolyte.<sup>[13]</sup> Therefore, this composite achieved specific capacity of 168 mAh g<sup>-1</sup> at  $0.1 \text{ A g}^{-1}$  and capacity retention of 96.7% after 5000 cycles at  $5 \text{ A g}^{-1}$ .<sup>[13]</sup> Another promising approach was carried out by Zaghib group by coating LTO by Li-rich organic layer by spray-dryer technique and compared with carbon coating.<sup>[14]</sup> The significant different were appeared at high rate where the Li-rich organic coated LTO provided

[a] M. M. Abdelaal, M. Alkhedher  
Mechanical and Industrial Engineering Department, Abu Dhabi University,  
P. O. Box 59911, Abu Dhabi, United Arab Emirates  
E-mail: mohammad.alkhedher@adu.ac.ae

 Supporting information for this article is available on the WWW under  
<https://doi.org/10.1002/batt.202400482>

superior capacity compared with pristine LTO and carbon coated LTO.<sup>[14]</sup> The majority of conductive polymers exhibit the capability to enhance ionic conductivity; however, they are limited in their ability to enhance electronic conductivity.<sup>[15]</sup>

In this context, our study aims to address these limitations by inducing self-doped  $Ti^{3+}$  and oxygen vacancies within LTO using Plasma Enhanced chemical vapor deposition (PECVD) for improving the internal conductivity. Subsequent carbon coating and an additional layer of Al-doped  $Li_7La_3Zr_2O_{12}$  (LLZO) to enhance the external electronic conductivity and facilitate the lithium-ion movement, respectively. The dual coating approach is expected to enhance both electronic and ionic conductivity while protecting active materials from side reactions and structural degradation at high rates. Therefore, the delivered capacity can be increased to reach the theoretical specific capacity of LTO (*i.e.*, 175 mAh g<sup>-1</sup>).<sup>[6]</sup>

## Experimental Section

### Materials

Commercial LTO was used as supplied (D90, 99% purity and tap density of 0.92 g cm<sup>-2</sup>, Nanografi Nano Technology) and Polyvinyl-pyrrolidone (PVP K-30, 12% nitrogen content, Hefei TNJ Chemical Industry Co., Ltd.) were used for carbon coating. Other materials include lithium hydroxide (LiOH, 98%, Thermo Scientific Chemicals), lanthanum oxide ( $La_2O_3$ , 99.99%, size: 325 mesh, Nanografi Nano Technology), zirconium oxide ( $ZrO_2$ , 99.99%, size: 325 mesh, American Elements), aluminum oxide ( $Al_2O_3$ , mesoporous, average pore size 3.8 nm, Sigma-Aldrich), and ethanol ( $C_2H_5OH$ , absolute, AR grade, 99.8%, Fisher Scientific) used for synthesizing Al-doped LLZO.

### Materials Synthesis

PECVD was employed to create oxygen vacancies and self-doped  $Ti^{3+}$  within LTO as detailed in the publication.<sup>[3]</sup> Specifically, 5 grams of commercial LTO underwent PECVD treatment in a tube furnace (200 Watt and 20 Pascal) at 400 °C in Ar/H<sub>2</sub> atmosphere for 1.5 h. The modified powder, named m-LTO, was manually ground to achieve homogeneous particles. To achieve carbon coating layer on LTO, a solution was prepared by sonicating 3 grams of m-LTP in a PVP solution (3 grams of PVP in 20 ml of deionized water) for 1 hour at room temperature. The resulting solution was then dried at 120 °C in an Ar gas environment for 2 hours, followed by a temperature increase to 450 °C to obtain m-LTO coated with a carbon layer, denoted as m-LTO@C. Various weight ratios of aluminum-doped lithium lanthanum zirconium oxide (Al-doped LLZO) were precipitated onto the m-LTO@C composite using conventional solid-state synthesis. Initially, LiOH-H<sub>2</sub>O,  $La_2O_3$ ,  $ZrO_2$ ,  $Al_2O_3$  were weighted according to the stoichiometric ratio of  $Li_{5.8}Al_{0.4}La_3Zr_2O_{12}$  as presented in Table S1, and the mixture was dispersed in ethanol before being placed in a zirconia jar. An excess of LiOH (10 wt.%) was added to compensate for anticipated lithium loss during the subsequent calcination process. The powders were ball-milled together for 12 hours at a speed of 300 rpm. Subsequently, 0.5 grams of m-LTO@C was added to the mixture and ball-milled for an additional 15 minutes. The resultant mixture was then transferred to an alumina crucible and heated at 120 °C for 12 hours. The temperature was subsequently increased to 1150 °C for 8 hours under argon flow to produce the m-LTO@C@Al-LLZO powder, referred to as LTO-L-x, with x (%) values of 0.5, 1.0, and 1.5

for simplicity.<sup>[16]</sup> The weight of Al-doped LLZO precursors was listed in Table S1. For comparison, Al-doped LLZO powder was synthesized using the same procedure in the absence of m-LTO@C. All samples were stored in an argon gas-filled glove box with oxygen and moisture levels maintained below 0.1 ppm and handling for characterization in a tight box containing Ar gas.

### Material Characterizations

The crystal structures of the synthesized materials were analyzed via X-Ray Diffraction (XRD) employing a Rigaku D/max-2500 X-ray generator, Cu  $\text{K}\alpha$  radiation, with operating conditions set at 40 kV and 1.5418 Å wavelength. Vibrational modes were assessed using a Raman microscope (DXR) equipped with a 532 nm laser beam, manufactured by Thermo-Fisher Scientific. Morphological features were examined through Field-Emission Scanning Electron Microscopy (FESEM) at 30 kV, utilizing a JEOL 7900F instrument, coupled with an Energy Dispersive X-Ray Analyzer (EDX) for elemental analysis. For a more detailed examination of the structure, Transmission Electron Microscopy (TEM) was performed using a Hitachi HT-7700 instrument. The samples were dispersed in ethanol, loaded onto copper grids, and allowed to dry naturally. This allowed for the visualization of the as-synthesized materials, coating layers, and the generation of highly magnified images. To investigate the elemental composition and binding states of surface elements, X-ray Photoelectron Spectroscopy (XPS) was performed using Al  $K\alpha$  radiation with a Scienta Omicron Multiprobe system, employing a 100  $\mu\text{m}$  aperture, pass energies of 150 eV for survey scans and 25 eV for high-resolution scans, a 50° takeoff angle, and averaging three scans for survey and ten scans for high-resolution analysis. Furthermore, Thermal Gravimetric Analysis (TGA) with a Q5000 analyzer was employed for thermal analysis of the weight of the carbon coating layer using alumina (aluminum oxide) crucibles. The analysis was conducted in air gas with a ramping rate of 5 °C per minute using 10 mg of samples, providing insights into the thermal stability of the coating layer.

### Electrode Preparation and Electrochemical Experiments

The electrodes were prepared by mixing the active material, Super P and polyvinylidene fluoride (PVDF) with a weight ratio of 8:1:1 while N-methyl-2-pyrrolidone (NMP) was used to adjust the viscosity of the slurry. Following magnetic stirring for 12 hours, the slurry was cast onto a copper foil, coated using a doctor-blade, and dried in a vacuum oven at 60 °C for 24 hours. The resulting electrode sheet underwent multiple calendaring steps and was subsequently punched into discs with dimensions of 1.33 cm<sup>2</sup>. The typical mass loading and thickness of these discs were approximately 3.5 mg cm<sup>-2</sup> and 43  $\mu\text{m}$ , respectively. Assembly of half-cells was conducted within an inert gas-filled glove box, employing the as-prepared electrode as the working electrode, lithium foil as a reference/counter electrode. The electrolyte, comprising 1 M LiPF<sub>6</sub> dissolved in a mixture of ethylene carbonate (EC) and diethyl carbonate (DEC) in a 1:1 volume ratio, was used in conjunction with a polyethylene separator.

Electrochemical measurements were carried out using a CHI 660E electrochemical workstation at room temperature. Prior to electrochemical tests, all cells underwent calendaring for 12 hours to attain a stable open circuit potential (OCP). Galvanic charge-discharge measurements were performed at various rates within a potential range spanning from 1.0 V to 2.5 V (*vs.* Li/Li<sup>+</sup>), allowing for a comprehensive assessment of the electrochemical performance. Electrochemical Impedance Spectroscopy (EIS) was performed at OCP from the frequency 100 kHz–100 mHz using a sinusoidal voltage of amplitude 5 V.

## 2. Results and Discussion

### 2.1. Characterization

The as-synthesized materials underwent thorough characterization utilizing various analytical tools to probe into crystal structure, chemical composition, and other pertinent properties. As shown in Figure 1, XRD patterns of m-LTO@C were matched with standard peaks of the cubic structure of LTO, exhibiting a space group of  $Fd\bar{3}m$  (JCPDS no. 49–207).<sup>[17,18]</sup> Distinctly, peaks at  $2\theta$  of  $18.3^\circ$ ,  $35.6^\circ$ ,  $43.2^\circ$ ,  $47.4^\circ$ ,  $57.2^\circ$ ,  $62.8^\circ$ , and  $66.1^\circ$ , were identified, corresponding to lattice planes of (111), (311), (400), (331), (333), (440), and (531), respectively.<sup>[13,17]</sup> The absence of other peaks implies that the plasma treatment successfully preserved the highly crystalline nature of LTO without inducing the formation of alternate phases such as  $Li_2O$  and  $TiO_2$ .<sup>[13]</sup> Additionally, the lack of peaks corresponding to carbon indicates the amorphous nature of the carbon coating layer.<sup>[19]</sup> Minor peaks, denoted by asterisks, emerged with the introduction of the second coating layer, attributed to Al-doped LLZO.<sup>[20–22]</sup>

The crystal structure of LLZO was further investigated by synthesizing Al-doped LLZO without m-LTO@C, revealing a cubic garnet structure for LLZO (JCPDS#45-109) as shown in Figure S1.<sup>[21,22]</sup> LLZO, known for its two crystal structures, tetragonal and cubic phase.<sup>[23]</sup> The former phase is thermodynamic stable at room temperature, but it shows poor ionic conductivity.<sup>[20,23]</sup> On contrast, the latter phase unstable and provides high conductivity.<sup>[23]</sup> Therefore, Al ions are doped inside the lattice of LLZO to stabilize the cubic phase during cooling.<sup>[20]</sup> Although 10% excess of lithium precursor was added to maintain the stoichiometry ratio necessary for the stabilization of the cubic phase of LLZO, a minor peak at 29 degrees appeared (\*), which indicates the formation of  $La_2Zr_2O_7$ .<sup>[24]</sup> The presence of cubic phase is crucial, as it offers significantly higher ionic conductivity compared to the tetragonal phase or any secondary phase such as  $La_2Zr_2O_7$ . This is indeed a consequence of lithium (Li) loss, a well-documented issue during the high-temperature synthesis of LLZO.<sup>[24–26]</sup> The

presence of  $La_2Zr_2O_7$  despite our precautions suggests that lithium loss exceeded the amount of excess LiOH added. It's also worth noting that aluminum (Al) incorporation, which can occur if there is a deficiency of lithium or at high temperatures, further complicates the phase stability.<sup>[27]</sup>

The structural features of cubic LLZO exhibit distinct vibration modes, as illustrated in Figure S2a. Peaks below  $150\text{ cm}^{-1}$  correspond to the  $T_{2g}$  and  $E_g$  vibration modes of La, while those shifted at  $258.5$  and  $296.4\text{ cm}^{-1}$  correspond to the  $T_{2g}$  and  $A_{1g}$  modes of oxygen-based vibrational bands.<sup>[28,29]</sup> Vibrations attributed to  $Li^+$  ion bonding occur at  $455.3\text{ cm}^{-1}$  and  $509.6\text{ cm}^{-1}$ , assigned to  $(E_g/T_{2g})$  and  $(T_{2g}/E_g)$  modes, respectively.<sup>[28,29]</sup> In addition, the  $A_{1g}$  stretching modes of Zr–O bond appeared at approximately  $\text{cm}^{-1}$ . These observations align with the characteristics of the cubic garnet structure of LLZO, as reported in the literature.<sup>[29,30]</sup> Additionally, the presence of a peak at  $1089\text{ cm}^{-1}$  is attributed to excess LiOH, either remaining from the precursors or forming before analysis in ambient air.<sup>[30]</sup>

On the other hand, in Figure S2b, the spinel structure of m-LTO exhibits five Raman phonon modes. Three peaks related to  $F_{2g}$  vibration ranging from  $200$ – $290\text{ cm}^{-1}$ , an  $E_g$  peak at  $430\text{ cm}^{-1}$ , and  $A_{1g}$  peak at  $677\text{ cm}^{-1}$  are observed.<sup>[17,18]</sup> A shoulder attached to the  $A_{1g}$  mode appears at  $740$ – $900\text{ cm}^{-1}$ .<sup>[13,17]</sup> The  $A_{1g}$  mode is associated with the phonon modes of bending vibrations of O–Ti–O bands in the  $TiO_6$  octahedron, while the  $E_g$  peak corresponds to the stretching vibrational mode of Li–O bands in the  $LiO_4$  tetrahedron.<sup>[18,31]</sup>  $F_{2g}$  stretching vibrational modes originate from the vibration of other Li–O bands, representing typical Raman vibrations of LTO.<sup>[13,18]</sup> Upon coating m-LTO with a carbon layer, two additional peaks related to disordered carbon (D-band at  $1340\text{ cm}^{-1}$ ) and the graphitic band (G-band at  $1598\text{ cm}^{-1}$ ) are detected (Figures 1b and S2b).<sup>[32]</sup> This indicates that the carbon layer is amorphous with some graphitic layer, potentially facilitating ion transport in the 2D direction.<sup>[32]</sup> It is noted that the intensity of D- and G- bands of LTO–L-x is significantly decreased, as compared to Figure S2c, after coating by LLZO as compared to m-LTO@C because LLZO layer acts as a physical barrier between the Raman laser and the carbon coating. Since

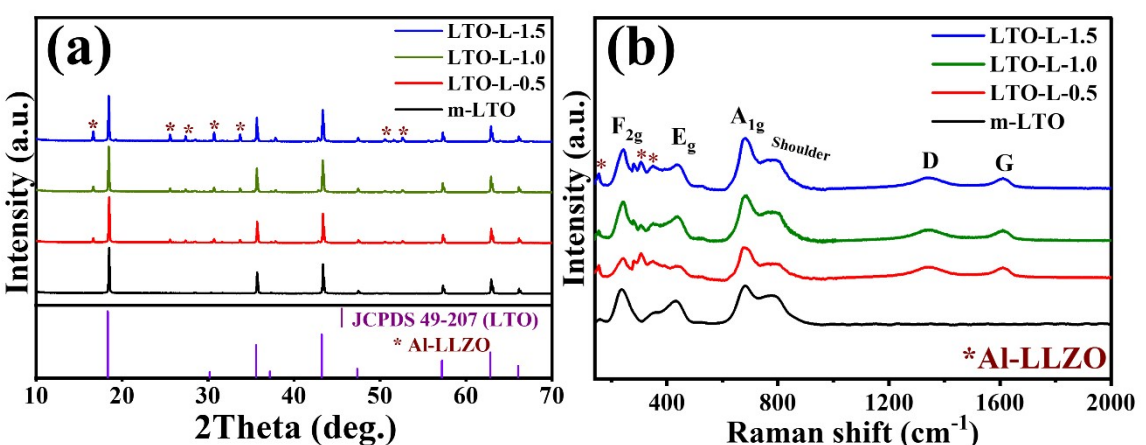


Figure 1. (a) XRD patterns and (b) Raman spectra of m-LTO and LTO-L-x, with x (%) values of 0.5, 1.0, and 1.5.

Raman scattering is a surface-sensitive technique, the additional LLZO layer can attenuate the Raman signal from the underlying carbon layer, leading to a decrease in the intensity of the D- and G-bands.

In addition, the absence of any Raman peaks corresponding to LiOH in the spectra of LTO–L-x suggests that the amount of residual LiOH is negligible. This observation further supports that the LiOH detected in the Raman analysis of pure Al-doped LLZO in Figure S2a is likely due to reactions with moisture in the environment rather than the presence of excess LiOH precursor. If the precursor had been sufficiently abundant, it would have prevented the formation of  $\text{La}_2\text{Zr}_2\text{O}_7$  by ensuring an adequate lithium supply to stabilize the desired phase. Following the coating with Al-doped LLZO, LTO–L-x materials exhibit combined characteristic peaks of LTO and LLZO (shown by asterisks in Figure 1b). The major peaks are assigned to LTO, while the minor peaks correspond to cubic LLZO. These results affirm the successful growth of cubic Al-doped LLZO on the surface of m-LTO@C. The findings provide conclusive evidence that cubic Al-doped LLZO has been effectively synthesized and grown on the surface of m-LTO@C.

The morphological analysis of m-LTO was conducted both before and after coating with carbon, as illustrated in Figure 2. Initially, the particles of m-LTO exhibited a spherical-like shape (Figure 2a), retaining the same morphology following the coating by carbon (Figure 2b). Such spherical particles provide

homogenous lithiation/delithiation process during cycling process and consequently few cracks.<sup>[33]</sup>

TEM images provided insights into the morphological alterations of different materials before and after modification. The *d*-spacing of 4.8 Å and 2.1 Å was measured, corresponding to the lattice planes of (111) and (400) of LTO, respectively, as shown in Figure 2c.<sup>[21,22]</sup> Subsequently, a new carbon layer of approximately 8 μm was observed, covering the LTO after the treatment with PVP (Figure 2d). As shown in Figure S3a the Al-doped LLZO did not change the morphology of particles. This indicates that the solid-state reaction did not induce changes in the original morphology. Different ratios of Al-doped LLZO layers were then presented in Figure 3. The carbon coating layer continued to cover the entire LTO lattice, while Al-doped LLZO exhibited varying thickness and homogeneity. With an increase in the ratio of Al-doped LLZO, the thickness increased until particle aggregation occurred. The LTO–L-0.5 an incomplete coverage with a thickness of approximately 1–2 μm, LTO–L-1.0 sample provided a uniform layer with a thickness of about 8–10 μm, and LTO–L-1.5 coating led to aggregated particles ranging from 5–15 μm. The observed incomplete coating at the 0.5 % level can be attributed to the insufficient mass of precursors, which adversely affected the uniformity of the coating, as illustrated in Figure 3d. Additionally, the deposition of LLZO onto m-LTO@C via the solid-state reaction presents inherent challenges due to the complexity of precursor materials derived from metal oxides. Consequently, a well-

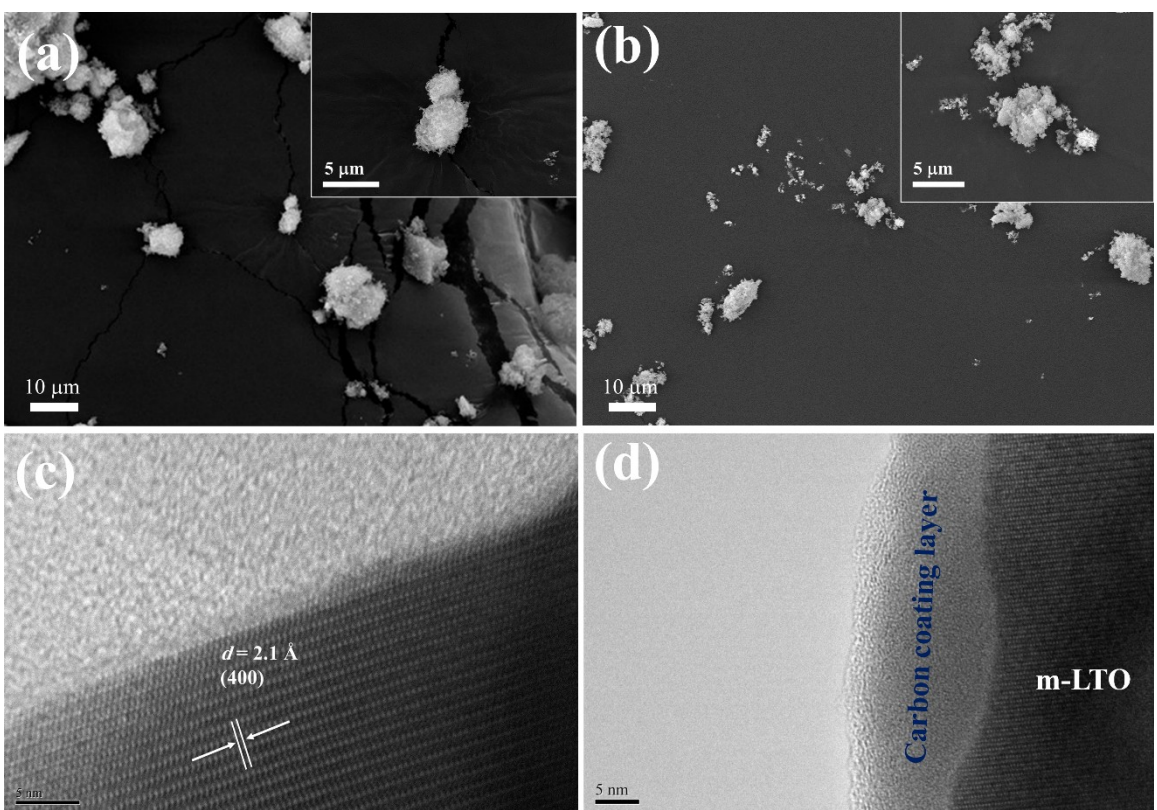


**Figure 2.** SEM images of (a) m-LTO and (b) m-LTO@C at a scale bar of 10 μm and TEM images of (c) m-LTO and (d) m-LTO@C at a scale bar of 5 nm. Inset: SEM images of (a) m-LTO and (b) m-LTO@C at a scale bar of 5 μm.

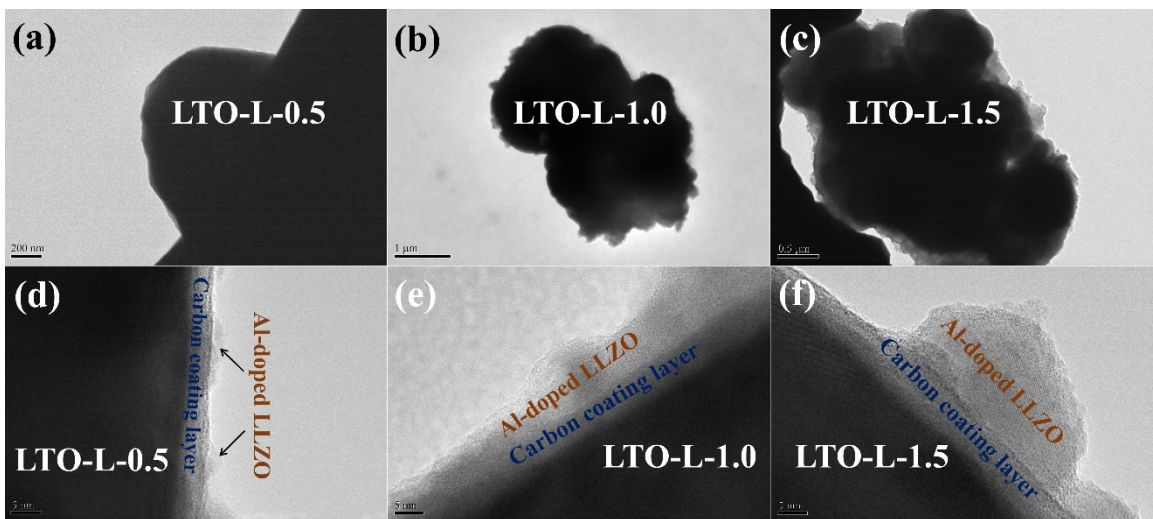


**Figure 3.** TEM images of (a and d) LTO–L-0.5, (b and e) LTO–L-1.0 and (c and f) LTO–L-1.5, with scale bars of (200 and 5) nm, respectively.

covered layer was only achieved at the 1.0% level, while higher percentages resulted in aggregation on the surface, as depicted in Figure 3f. A uniform coating layer is expected to contribute to stable performance during the charge-discharge process, providing effective protection and ensuring long cycling life.<sup>[34,35]</sup>

Elemental analysis of LTO–L-1.0 in Figure S3b confirms the presence of O, Zr, Ti, La, Al, and C elements, indicating the existence of the carbon layer and Al doping. No nitrogen signal was detected by EDX due to minor nitrogen content in the precursor of carbon (*i.e.*, PVP). These signals match the XRD pattern and TEM images of LTO coated by carbon and cubic phase of Al-doped LLZO.

The surface analysis of LTO–L-1.0 was performed using XPS to investigate the oxidation states of various elements in the composite. The corresponding spectra of La, Ti, O, C, Zr, Al, and Li were observed, confirming the chemical composition of the LTO-based composite, including Al-doped LLZO and carbon coating (Figure S4a).<sup>[36,37]</sup> Deconvolution of the C 1s peaks at 284.5 eV, 285.8 eV, and 289.5 eV (Figure 4a) established the presence of C–C bond, C–O/C–N bonds, and O–C=O group, respectively, all indicative of the chemical composition of the carbon layer.<sup>[36,38]</sup> The O 1s peak at 530 eV suggested the possibility of Li<sub>2</sub>O formation, potentially evolving into Li<sub>2</sub>CO<sub>3</sub> upon LLZO exposure to air.<sup>[36,39]</sup> However, XRD analysis did not detect peaks corresponding to Li<sub>2</sub>O or Li<sub>2</sub>CO<sub>3</sub>, indicating negligible amounts of these by-products.<sup>[39]</sup> Additionally, a deconvoluted peak at 531.5 eV indicated oxygen vacancies resulting from Al doping, inducing defects and vacancies in the LLZO lattice.<sup>[37]</sup>

The Ti 2p spectrum of LTO–L-1.0 displayed characteristic peaks ( $2p_{1/2}$  and  $2p_{3/2}$ ), each deconvoluted into two peaks corresponding to the oxidation states 3+ and 4+ of titanium (Figure 4c).<sup>[3]</sup> This transition between oxidation states may enhance the internal electronic conductivity of LTO during the charge-discharge process.<sup>[3,38]</sup> In contrast, the unmodified LTO shows only 4+ oxidation state in Figure 4e, confirming the

successful induction of Ti<sup>3+</sup> through the PECVD process. The presence of Al 2p at a binding energy of 74.8 eV stabilizes the cubic crystal structure of LLZO during cooling, preventing the conversion to a less conductive tetragonal structure.<sup>[20,37]</sup>

The proportion of the carbon layer in the LTO–L-x composites was determined by TGA (Figure 4Sb) compared to m-LTO and m-LTO@C. As seen, m-LTO showed high thermal stability with air until 600 °C, while the coated one by carbon started to burn from 250–450 °C. After coating by Al-doped LLZO, the thermal stability extended to ~370 °C, followed by a 3–5% decrease due to the ignition of the carbon coating layer in the presence of air. The presence of voids between grains of Al-doped LLZO allows oxygen to penetrate and reaction with carbon layer during test.<sup>[40]</sup>

## 2.2. Electrochemical Performance

Our composites design, incorporating various ratios of Al-doped LLZO, underwent testing for lithium storage in half-cells, evaluating delivered capacity and cyclability. The m-LTO electrode exhibited a plateau during lithium insertion/extraction in the olivine structure at 1.55 V (vs. Li/Li<sup>+</sup>) (Figure S5a). In the spinel LTO, which stores 3Li<sup>+</sup> and undergoes conversion to the rock-salt phase (Li<sub>7</sub>Ti<sub>5</sub>O<sub>12</sub>), the oxidation state of Ti experiences a reduction from 4+ to 3+. It is noteworthy that the lattice parameters of both LTO and Li<sub>7</sub>Ti<sub>5</sub>O<sub>12</sub> are remarkably similar, and the lattice contraction following lithiation is negligible.<sup>[6]</sup> Consequently, lithium titanate exhibits prolonged cycling performance compared to other materials.<sup>[6]</sup>

Coating with a carbon layer (Figure S5b) enhanced electron movement over the outer surface, leading to an elongated voltage plateau.<sup>[41]</sup> Consequently, the delivered capacity exhibited a notable increase from 153.2 mAh g<sup>-1</sup>–165.5 mAh g<sup>-1</sup>, accompanied by an enhancement in initial Coulombic efficiency from 96%–97% at 0.1 A g<sup>-1</sup>. This underscores the pivotal role of electronic conductivity in optimizing the performance of oxide-

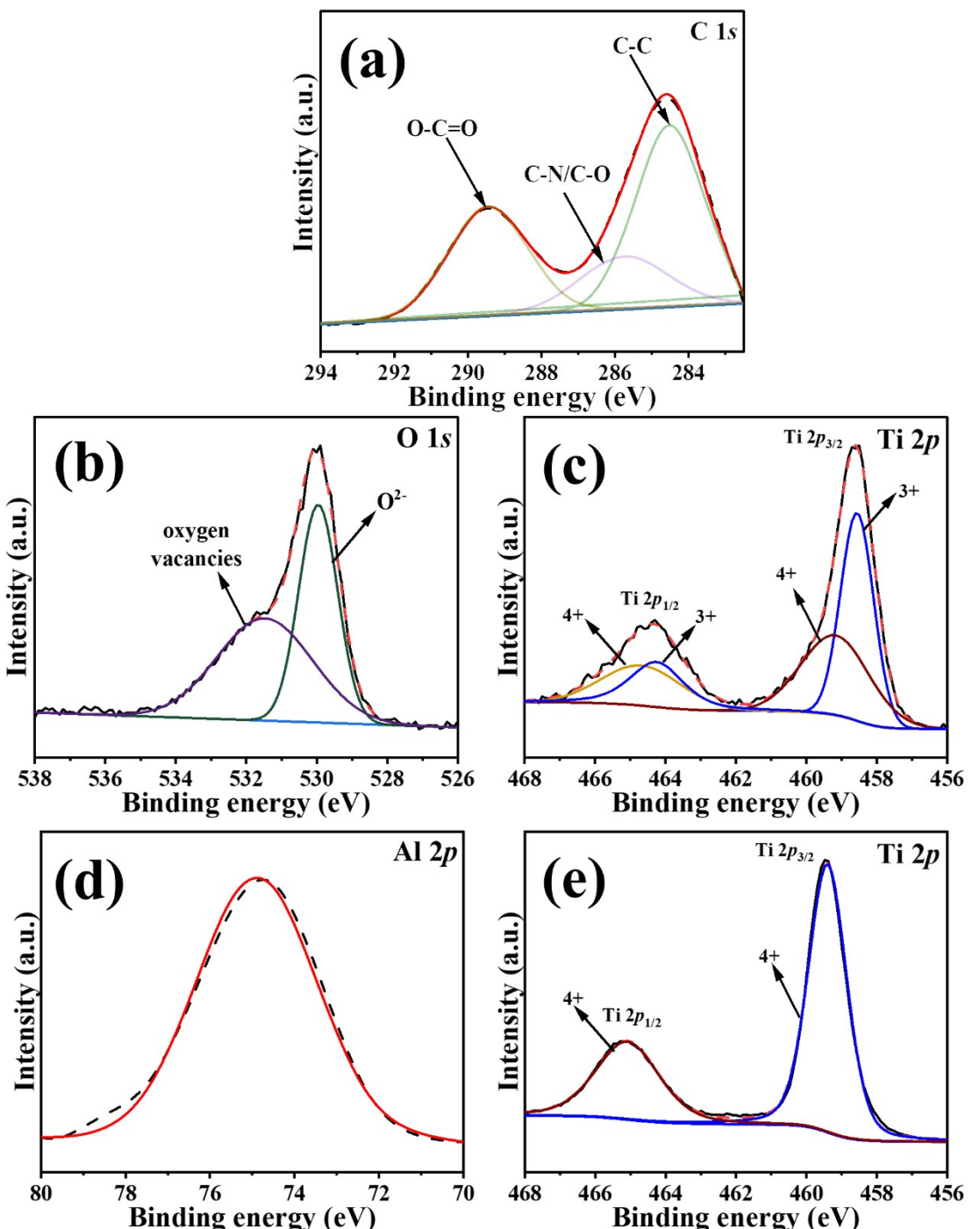


**Figure 4.** XPS analysis of LTO–L-1.0 nanocomposite: high-resolution spectra of (a) C 1s, (b) O 1s, (c) Ti 2p and (d) Al 2p, alongside (e) the Ti 2p spectrum of unmodified LTO for comparison.

based active materials, such as LTO.<sup>[4,9]</sup> Additionally, the carbon layer played a crucial role in mitigating the formation of SEI by impeding direct contact between electrolyte components and the LTO crystal.<sup>[41,42]</sup> The introduction of Al-doped LLZO in the coating process further strengthened these desirable characteristics (Figure 5a).

Galvanic charge-discharge (GCD) profiles of LTO–L-0.5 and LTO–L-1.0 resembled m-LTO and m-LTO@C, while LTO–L-1.0

exhibited a flatter, longer plateau, indicating enhanced lithium-ion storage. LTO–L-1.5 displayed the smallest delivered capacity, a distorted voltage profile, and higher polarization, possibly linked to the inhomogeneity of the Al-doped LLZO coating layer observed in TEM images.<sup>[13]</sup> Initial Coulombic efficiencies for LTO–L-0.5, LTO–L-1.0, and LTO–L-1.5 at 0.1 A g<sup>-1</sup> were 99.0%, 97.7%, and 98.1%, respectively, suggesting some lithium ions formed SEI and were trapped in the Al-doped LLZO

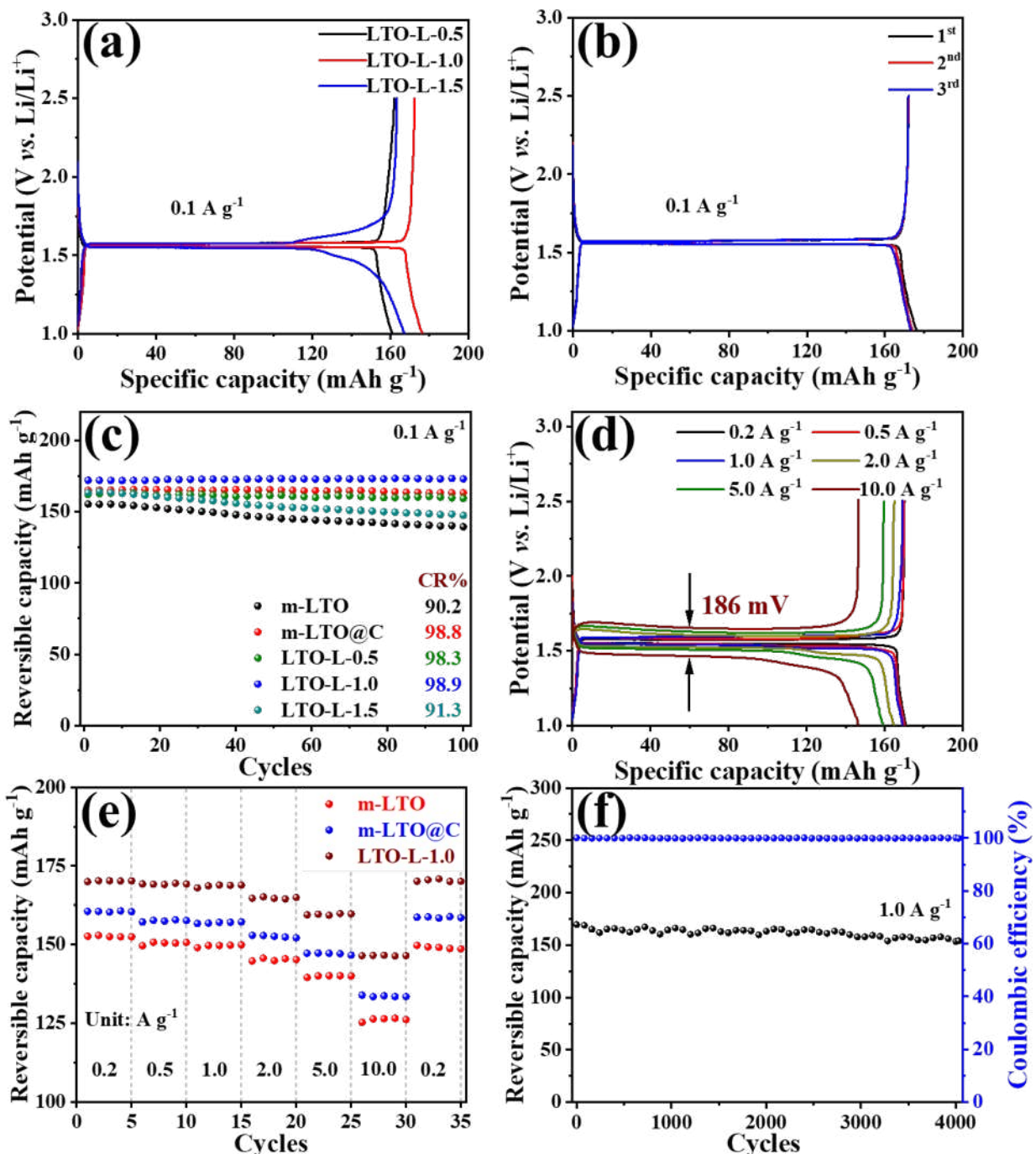


**Figure 5.** (a) Initial GCD profiles of LTO–L-x at the current density of  $0.1 \text{ A g}^{-1}$ , (b) first three GCD profiles of LTO–L-1.0 at the current density of  $0.1 \text{ A g}^{-1}$ , (c) cyclic stability test at a current density of  $0.1 \text{ A g}^{-1}$ , (d) GCD profiles of LTO–L-1.0 at various rates from  $0.2$ – $10.0 \text{ A g}^{-1}$ , (e) the corresponding reversible capacities and (f) cyclic stability test of LTO–L-1.0 at a current density of  $1.0 \text{ A g}^{-1}$ . Tests in (c), (d) and (f) were conducted after three cycles at  $0.1 \text{ A g}^{-1}$ .

layer during the first lithiation reaction.<sup>[13,14]</sup> After three cycles at  $0.1 \text{ A g}^{-1}$ , Coulombic efficiency restored to 99.9%, demonstrating stable reversible capacity, particularly for the LTO–L-1.0 sample (Figure 5b).<sup>[20]</sup>

Cycling stability tests at a current rate of  $0.1 \text{ A g}^{-1}$  for 100 cycles (Figure 5c) showed that m-LTO experienced a capacity

retention (CR) of 90.2%, while LTO@C exhibited superior improvement in CR to reach 98.8%. Coated samples LTO–L-0.5 and LTO–L-1.0 provided similar CR of 98.3% and 98.9% due to inhibit the SEI formation, indicating the ease of lithium-ion movement inside the m-LTO lattice by an additional coating layer of Al-doped LLZO, without causing degradation.<sup>[13]</sup> In

contrast, LTO–L-1.5 showed a CR of 91.3%, similar to m-LTO without any coating layer, potentially due to an aggregated coating layer causing inhomogeneous lithiation, leading to the formation of an unstable SEI and ongoing cracking.<sup>[43]</sup> The capacity retention of m-LTO@C is like that of LTO–L-0.5 and LTO–L-1.0, suggesting that the 0.5% and 1.0% LLZO coatings do not significantly degrade performance. The 1.0% LLZO coating, however, achieves an optimal balance by providing sufficient coverage and enhancing electrochemical performance without introducing substantial resistance or aggregation. Consequently, LTO–L-1.0 demonstrates superior capacity compared to LTO–L-0.5 and m-LTO@C. The 1.0% LLZO coating represents the best compromise between coverage and conductivity, leading to improved performance. In contrast, the 0.5% LLZO coating offers incomplete protection, while the 1.5% coating results in aggregation that adversely affects performance.

Rate capability tests spanning from  $0.2 \text{ A g}^{-1}$ – $10.0 \text{ A g}^{-1}$  were conducted to assess the high-rate performance of LTO–L-1.0 (Figure 5d) in comparison with m-LTO (Figure S5c) and m-LTO@C (Figure S5d). While the polarization gap between charge and discharge plateaus was negligible at low rates, it was observed that, at  $10.0 \text{ A g}^{-1}$ , the gap decreased from 259 mV for m-LTO to 209 mV and 186 mV for m-LTO@C and LTO–L-1.0, respectively. The reduction in polarization observed can be attributed to the enhancement of electronic conductivity through carbon coating and the facilitation of lithium-ion movement via Al-doped LLZO coating.<sup>[23,41]</sup>

The reversible capacities at low rates are comparable to each other due to improve the internal electronic conductivity by  $\text{Ti}^{3+}$  self-doped.<sup>[3]</sup> Consequently, LTO–L-1.0 exhibited higher delivered capacity at various current rates compared to m-LTO and m-LTO@C (Figure 5e). Notably, LTO–L-1.0 demonstrated capacities of 170.3, 169.3, 168.9, 165, 159.8, and  $146.5 \text{ mAh g}^{-1}$  at current rates of 0.2, 0.5, 1.0, 2.0, 5.0, and  $10 \text{ A g}^{-1}$ . The delivered capacity at high rates for LTO–L-1.0 was significantly higher than that of m-LTO and m-LTO@C, underscoring the dual coating layer's ability to facilitate fast charge-discharge processes and deliver high power.<sup>[36,37]</sup> Additionally, the recovered capacity of LTO–L-1.0 at a rate of  $0.2 \text{ A g}^{-1}$  was  $170.1 \text{ mAh g}^{-1}$ , indicating the high stability of our composite even after experiencing high current rates.<sup>[44]</sup>

To assess the impact of modified LTO materials on charge transfer resistance, Electrochemical Impedance Spectroscopy (EIS) was conducted for LTO, m-LTO, m-LTO@C, and LTO–L-1.0 electrodes, as shown in Figure S6. The equivalent circuit model used to fit the EIS spectra is depicted in inset Figure S6, where  $R_b$  represents bulk transfer resistance, and  $R_{ct}$  represents charge transfer resistance. As indicated by the fitting data in Table S2, the  $R_{ct}$  value of m-LTO is lower than LTO that of unmodified LTO, which is attributed to the introduction of  $\text{Ti}^{3+}$ , enhancing the internal electronic conductivity. Subsequent carbon coating further reduces  $R_{ct}$  to 85.2 ohms by improving external conductivity and facilitating better connections between LTO particles. Finally, the application of an Al-doped LLZO layer decreases  $R_{ct}$  to 45.3, owing to enhanced ionic conductivity. These results indicate that each modification of the LTO

**Table 1.** Comparison of the electrochemical performance of modified LTO materials reported in the literature.

Materials	Rate/CR (%)-@Cycles	Capacity ( $\text{mAh g}^{-1}$ )	Ref.
LTO@ $\text{Li}_x\text{TiO}_2$	1 C/ 95.2@400	175.1@0.05 C	[34]
La-doped LTO	5 $\text{A g}^{-1}$ / 85.7@1,000	145.2@0.2 $\text{A g}^{-1}$	[46]
Ce-doped LTO	5 $\text{A g}^{-1}$ / 86.6@1,000	177.2@0.2 $\text{A g}^{-1}$	[46]
F-doped LTO@NC	0.5 $\text{A g}^{-1}$ / 95.0@2,000	175.0@0.1 A/g	[10]
I-doped LTO	1 C/ 99.2@100	172.2@0.5 C	[47]
Carbon coated ultrathin nanosheet LTO	10 C/ 77.2@10,000	166.5@0.5 C	[48]
C-coated Fe-doped LTO	5 C/ 92.6@1,000	172.2@0.2 C	[1]
Al-doped LLZO@C@LTO	1.0 A/g/ 90.8@4,000	165.5@0.1 A/g	This study

contributes to improved overall conductivity, thereby explaining the observed enhancement in delivered capacities.

Encouraged by these promising performance outcomes, long cycling stability was investigated at a rate of  $1.0 \text{ A g}^{-1}$  (Figure 5f). The composite LTO–L-1.0 exhibited a capacity retention (CR) of 90.8% after 4000 cycles, with Coulombic efficiency close to 99%. The uniformity of dual coating layer provides homogenous stress distribution along with the particles, resulting in effective protection against degradation and cracking during lithium intercalation and deintercalation.<sup>[44,45]</sup> The electrochemical performance was compared to other literature as seen in Table 1. Al-doped LLZO@C@LTO demonstrates competitive electrochemical performance compared to other modified LTO materials reported in the literature. This performance is particularly impressive when considering the superior long-term stability, highlighting the effectiveness of the Al-doped LLZO and carbon coating in enhancing the electrochemical properties of LTO. The findings underscored the ability of these coating layers to sustain high electronic and ionic conductivity even during extended cycling at high current rates, positioning the composite as a promising candidate for long-term cycling applications.

### 3. Conclusions

In conclusion, our study presents a comprehensive investigation into the design, synthesis, and performance evaluation of a composite material for lithium-ion battery applications. The synthesis involved employing PECVD to create oxygen vacancies and self-doped  $\text{Ti}^{3+}$  within lithium titanium oxide (LTO), followed by carbon coating and Al-doped lithium lanthanum zirconate garnet (LLZO) layer deposition. Various characterization techniques, including XRD, Raman spectroscopy, SEM, TEM, XPS, and TGA, were employed to analyze the crystal

structure, morphology, and composition of the synthesized materials. The results confirmed the successful creation of the desired structures, with Al-doped LLZO coating on carbon-coated LTO, validating the effectiveness of the synthesis approach. The Al-doped LLZO coating composition was systematically optimized based on electrochemical performance as anode materials. The dual coating layers significantly improved the rate capability, reducing polarization gaps and enabling higher delivered capacities at various current rates. Long cycling stability tests demonstrated that the LTO–L-1.0 composite maintained a high-capacity retention, affirming the robustness of the coating layers and their ability to sustain high electronic and ionic conductivity even during prolonged cycling.

## Acknowledgements

This research is supported by ASPIRE, the technology program management pillar of Abu Dhabi's Advanced Technology Research Council (ATRC), via the ASPIRE "VRI (Virtual Research Institute)".

## Conflict of Interests

The authors declare no conflict of interest.

## Data Availability Statement

The data that support the findings of this study are available in the supplementary material of this article.

**Keywords:** Anode materials • Conductivity • Lithium titanate • High rate • Al-doped LLZO

- [1] X. Jiang, G. Ma, Q. Zhu, H. Ge, Q. Chen, B. Yan, L. Deng, C. Tian, C. Wu, *Sci. Rep.* **2023**, *13*, 15118.
- [2] Y. Liu, H. Shi, Z.-S. Wu, *Energy Environ. Sci.* **2023**, *16*, 4834–4871.
- [3] K. Liang, H. He, Y. Ren, J. Luan, H. Wang, Y. Ren, X. Huang, *Ionics* **2020**, *26*, 1739–1747.
- [4] S. Qing-feng, W. Xian-ming, W. Xian-wen, W. Zhi-ru, L. Jing-li, *Ionics* **2020**, *26*, 2217–2223.
- [5] J. Liu, A. Wei, G. Pan, S. Shen, Z. Xiao, Y. Zhao, X. Xia, *J. Energy Chem.* **2021**, *54*, 754–760.
- [6] H. Zhang, Y. Yang, H. Xu, L. Wang, X. Lu, X. He, *InfoMat* **2022**, *4*, e12228.
- [7] X. Jin, Y. Han, Z. Zhang, Y. Chen, J. Li, T. Yang, X. Wang, W. Li, X. Han, Z. Wang, *Adv. Mater.* **2022**, *34*, 2109356.
- [8] K. Govindarajan, R. N. Nasara, S.-K. Lin, *Batter. Supercaps.* **2022**, *5*, e20220010.
- [9] L. Zuo, D. Lu, T. Yang, D. Yue, W. Li, Q. Ma, Y. Chen, C. Zheng, X. Wu, *Carbon Neutralization* **2022**, *1*, 316–345.
- [10] Z. Zhang, S. Lu, G. Huang, W. Wang, D. He, Y. Liu, F. Gao, Y. Chen, H. Zhan, J. Mei, M. Terrones, Y. Wang, X. Chen, *Carbon* **2024**, *221*, 118885.
- [11] Z. N. Ezyeh, M. Khodaei, F. Torabi, *Ceram. Int.* **2023**, *49*, 7105–7141.
- [12] Z. Wang, W. Yang, J. Yang, L. Zheng, K. Sun, D. Chen, L. Sun, X. Liu, *Ceram. Int.* **2020**, *46*, 12965–12974.
- [13] T. Zhu, C. Yu, Y. Wu, Y. Wang, *ACS Sustainable Chem. Eng.* **2023**, *11*, 482–490.

- [14] N. Delaporte, P. Chevallier, S. Rochon, G. Lajoie, J.-C. Daigle, V. Gariepy, D. Clément, R. Veillette, M.-C. Mathieu, M. Provencher, M. L. Trudeau, K. Zaghib, *Mater. Adv.* **2020**, *1*, 854–872.
- [15] A. K. Poddar, S. S. Patel, H. D. Patel, *Polym. Adv. Technol.* **2021**, *32*, 4616–4641.
- [16] X. Ping, Q. Zheng, B. Meng, W. Lin, Y. Chen, C. Fang, H. Zhang, W. Liang, *Ceram. Int.* **2022**, *48*, 25689–25695.
- [17] P. Ahmed, W. Ghann, J. Uddin, M. A. Yousuf, *SN Appl. Sci.* **2022**, *4*, 111.
- [18] C.-F. Xiao, J. H. Kim, D. Choi, Y. C. Park, J. H. Kim, J. Park, Y. J. Kim, H.-S. Kim, *J. Alloys Compd.* **2019**, *801*, 550–557.
- [19] C. Liang, Y. Chen, M. Wu, K. Wang, W. Zhang, Y. Gan, H. Huang, J. Chen, Y. Xia, J. Zhang, *Nat. Commun.* **2021**, *12*, 119.
- [20] C. Chen, K. Wang, H. He, E. Hanc, M. Kotobuki, L. Lu, *Small* **2023**, *19*, 2205550.
- [21] O. Sreejith, R. Murugan, *J. Alloys Compd.* **2023**, *939*, 168774.
- [22] T. Li, P. K. Panda, C.-T. Hsieh, Y. A. Gandomi, P.-C. Yang, *J. Energy Storage* **2024**, *81*, 110444.
- [23] M. M. Raju, F. Altayran, M. Johnson, D. Wang, Q. Zhang, *Electrochem* **2021**, *2*, 390–414.
- [24] Y. Zhou, X. Li, Y. Yang, X. Huang, B. Tian, *ACS Appl. Energy Mater.* **2022**, *5*, 13817–13828.
- [25] Y. Zhang, D. Luo, W. Luo, S. Du, Y. Deng, J. Deng, *Electrochim. Acta* **2020**, *359*, 136965.
- [26] M. Botros, J. Gonzalez-Julian, T. Scherer, R. Popescu, C. Loho, A. Kilmametov, O. Clemens, H. Hahn, *Batter. Supercaps.*, e202300370.
- [27] J. Košir, S. Mousavihasemi, B. P. Wilson, E.-L. Rautama, T. Kallio, *Solid State Ion.* **2022**, *380*, 115943.
- [28] Z. Liu, A. Borodin, F. Endres, *Energy Technology* **2022**, *10*, 2100907.
- [29] S. A. Pervez, G. Kim, B. P. Vinayan, M. A. Cambaz, M. Kuenzel, M. Hekmatfar, M. Fichtner, S. Passerini, *Small* **2020**, *16*, 2000279.
- [30] F. Rahmawati, B. Musyarofah, K. D. Nugrahaningtyas, A. Prasetyo, V. Suendo, H. Haeruddin, M. F. A. Handaka, H. Nilasari, H. Nursukatmo, *J. Mater. Res. Technol.* **2021**, *15*, 2725–2734.
- [31] H. A. Llán-Jiménez, D. A. Buchberger, M. Winkowska-Struzik, M. Ratyński, M. Krajewski, M. Boczar, B. Hamankiewicz, A. Czerwiński, *Batteries* **2022**, *8*, 168.
- [32] R. Kumar, A. Soam, V. Sahajwalla, *Mater. Adv.* **2021**, *2*, 2918–2923.
- [33] X. Zhu, Y. Chen, H. Chen, W. Luan, *Int. J. Mech. Sci.* **2020**, *178*, 105608.
- [34] E. J. Moon, J. K. Hong, S. K. Mohanty, M. Yang, K. Ihm, H. Lee, H. D. Yoo, *J. Power Sources* **2023**, *559*, 232657.
- [35] J. Bae, J. Ji, M. Kim, S. K. Kang, G. H. Park, Y. H. Jeong, C. Jo, W. B. Kim, *Energy Fuels* **2023**, *37*, 12445–12456.
- [36] W. Xia, B. Xu, H. Duan, Y. Guo, H. Kang, H. Li, H. Liu, *ACS Appl. Mater. Interfaces* **2016**, *8*, 5335–5342.
- [37] Y. Zhu, J. Zhang, W. Li, Y. Xue, J. Yang, S. Li, *Ceram. Int.* **2023**, *49*, 10462–10470.
- [38] Y. Wang, Y.-X. Zhang, W.-J. Yang, S. Jiang, X.-W. Hou, R. Guo, W. Liu, P. Huang, J. Lu, H.-T. Gu, J.-Y. Xie, *J. Electrochem. Soc.* **2019**, *166*, A5014.
- [39] Z. Liu, G. Li, A. Borodin, X. Liu, Y. Li, F. Endres, *J. Solid State Electrochem.* **2019**, *23*, 2107–2117.
- [40] G. Ferraresi, S. Uhlenbrück, C.-L. Tsai, P. Novák, C. Villevieille, *Batter. Supercaps.* **2020**, *3*, 557–565.
- [41] J. Gong, X. Zeng, X. Zhou, R. Shi, K. Xia, K. Huang, *J. Electroanal. Chem.* **2024**, *952*, 117932.
- [42] H. J. Kim, J. H. Jo, J. U. Choi, N. Voronina, D. Ahn, T.-Y. Jeon, H. Yashiro, Y. Aniskevich, G. Ragoisha, E. Streltsov, S.-T. Myung, *Energy Storage Mater.* **2021**, *40*, 197–208.
- [43] X. Bai, T. Li, Y.-J. Bai, *Dalton Trans.* **2020**, *49*, 10003–10010.
- [44] S. Geng, Y. Zhang, B. Xie, A. Shi, Y. Ning, S. Lou, G. Yin, *J. Phys. Chem. C* **2023**, *127*, 15021–15034.
- [45] J. Kang, H. R. Shin, J. Yun, S. Kim, B. Kim, K. Lee, Y. Lim, J.-W. Lee, *Energy Storage Mater.* **2023**, *63*, 103049.
- [46] M. Qin, Y. Li, X.-J. Lv, *Nanomaterials (Basel)* **2017**, *7*, 150.
- [47] L. Noerochim, R. S. Prabowo, W. Widayastuti, D. Susanti, A. Subhan, N. H. Idris, *Batteries* **2023**, *9*, 38.
- [48] Y. Hu, L. Wang, C. Zhu, L. Zhang, C. Wang, *Appl. Surf. Sci.* **2024**, *656*, 159619.

Manuscript received: July 13, 2024  
 Revised manuscript received: September 14, 2024  
 Accepted manuscript online: September 17, 2024  
 Version of record online: October 30, 2024